Title
Design Considerations and Experimental Characterization of Plasmonic Metamaterial Absorbers for Selective Infrared Sensing

Author
Rowe, Jeremy Adam

Publication Date
2022

Peer reviewed|Thesis/dissertation

Design Considerations and Experimental Characterization of Plasmonic Metamaterial Absorbers for Selective Infrared Sensing

By

JEREMY ADAM ROWE

THESIS

Submitted in partial satisfaction of the requirements for the degree of

MASTER OF SCIENCE

in

Electrical and Computer Engineering

in the

OFFICE OF GRADUATE STUDIES

of the

UNIVERSITY OF CALIFORNIA

DAVIS

Approved:

Juan Sebastian Gomez-Diaz, Chair

William Putnam

Weijian Yang

Committee in Charge

2021

Abstract—

Metamaterial absorbers are devices made from arrays of subwavelength structures used to manipulate electromagnetic radiation incident upon them and they are becoming increasingly important with the implementation of the internet of things and the ubiquity of sensors present in everyday life. This research presents experimental methods to measure the performance of micro and nano electromechanical systems (MEMS/NEMS) produced by our research group. A series of simulations were performed using COMSOL, Ansys HFSS, and Python to provide predictions of their performance. An experimental LabVIEW setup is also presented to measure the performance of a plasmonic piezoelectric NEMS resonator, while various MEMS absorbers were analyzed using Fourier transform infrared spectroscopy. Various considerations are presented for the materials used in the production of these devices, and their application to use in the sensing of biological and gaseous systems is also discussed. The experimental measurements provided here confirm their potential application as low cost, high resolution, uncooled detectors.

Keywords— metasurface, MEMS, NEMS, infrared detector, resonator, metamaterial absorber

Design Considerations and Experimental Characterization of Plasmonic Metamaterial Absorbers for Selective Infrared Sensing

By: J.A. Rowe
Electrical and Computer Engineering Department, University of California Davis, Davis, CA, USA
jerrowe@ucdavis.edu
Supervised by: Dr. J. S. Gomez Diaz
Electrical and Computer Engineering Department, University of California Davis, Davis, CA, USA

I. INTRODUCTION

With the increasing ubiquity of sensors in our everyday devices and the popularization of the internet of things, the availability of uncooled, high-resolution detectors is exceedingly important. Various micro and nano electromechanical systems (NEMS/MEMS) are currently being developed at the Applied Micro/Nano-Electromagnetics Research Laboratory, and the results here are presented to confirm their performance. The goal of the research presented here is to also determine the parameter space of available materials and orientation of metasurface arrays that can be used to effectively tune the electromagnetic absorption of a metasurface for infrared detection.

Various simulations were used to characterize these metasurfaces and to predict their performance using COMSOL, Ansys HFSS, and a lumped circuit model implemented using Python. The simulations analyzed a previously employed cross metasurface, but also analyzed other possibilities, such as a nested ring structure and Fano-resonances to achieve similar results. While gold and silicon dioxide are currently the most explored materials in the laboratory setting, additional metals are explored for future attempts at making lower cost devices that could be expanded to a larger application of the technology.

An optical experiment automated using LabVIEW is presented in measurement of the phase shift generated by a plasmonic piezoelectric NEMS resonator. Finally, evidence is presented which shows the applicability of these technologies to the measurement of gaseous and biological samples.

II. Circuit Model Approximation

A lumped circuit model and transmission line approach was used to determine the absorption and FWHM of various metal-insulator-metal (MIM) metamaterial absorbers. This approach can be used to quickly calculate the performance of a metasurface with minimal computing requirements using Python. The parameters used in the circuit model are shown in the equations and in Figure 01 below. [1,6]

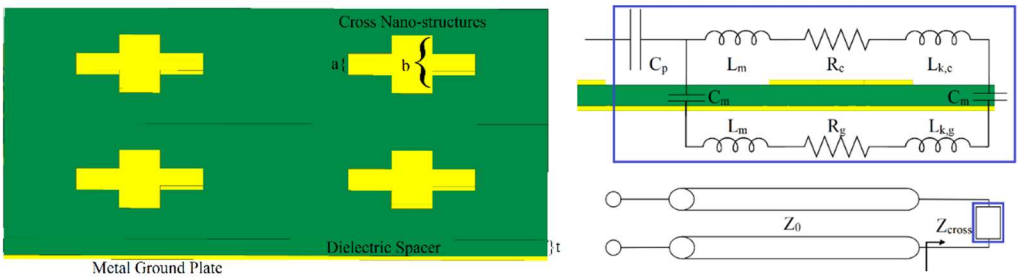

Figure 01: Metal Insulator Metal (MIM) metamaterial absorber shown with cross arm width 'a' and cross width 'b' and a varying thickness dielectric 't' and periodicity Λ (LEFT). The absorber impedance is calculated using a lumped circuit model and transmission line model (RIGHT). [6]

$$C_p = \frac{\pi \varepsilon_0 a}{\ln\left(\frac{2\Lambda - b}{t_{metal}} + \sqrt{\left(\frac{2\Lambda - b}{t_{metal}}\right)^2 - 1}\right)} \quad (1)$$

$$L_m = \frac{1}{2}\mu_0 \, t_{oxide} \, \frac{b}{a} \quad (2)$$

$$C_m = c\,\frac{1}{2}\varepsilon_0 \varepsilon_{oxide} \, \frac{ba}{2t_{oxide}} \quad (3)$$

$$R_C = \frac{c\prime b}{a\delta_{metal}\sigma_{metal}} \quad (4)$$

$$R_g = \frac{b}{0.5b\delta_{metal}\sigma_{metal}} \quad (5)$$

$$L_{k,c} = \frac{c\prime b}{a\delta_{metal}\varepsilon_0\omega_p^2} \qquad (6)$$

$$L_{k,g} = \frac{b}{0.5b\delta_{metal}\varepsilon_0\omega_p^2} \qquad (7)$$

The Lorentz-Drude (LD) model was used to analyze the permittivity of various metals considered for the production of these metasurfaces. The LD model examines the electron as a harmonic oscillator and uses the plasma frequency and damping coefficients of the material to determine the permittivity within the infrared spectrum. The three metals being considered are aluminum, copper, and gold. Gold has been the primary material previously used in this research as its reflectivity and ease in polishing is ideal for laboratory conditions. However, the high cost of gold makes it less than ideal for products, and so copper and aluminum are examined here as potential replacements which have similar permittivity in the infrared range. The permittivity of each metal was calculated using Python with the LD model comprised of the following equations and the results are shown below in Figure 02. [10]

$$\varepsilon_r(\omega) = \varepsilon_r^{(f)}(\omega) + \varepsilon_r^{(b)}(\omega) \qquad (8)$$

$$\varepsilon_r^{(f)}(\omega) = 1 - \frac{\Omega_p^2}{\omega(\omega - i\,\Gamma_0)} \qquad (9)$$

$$\varepsilon_r^{(b)}(\omega) = \sum_{j=1}^{k} \frac{f_j\omega_p^2}{(\omega_j^2 - \omega^2) + i\omega\Gamma_j} \qquad (10)$$

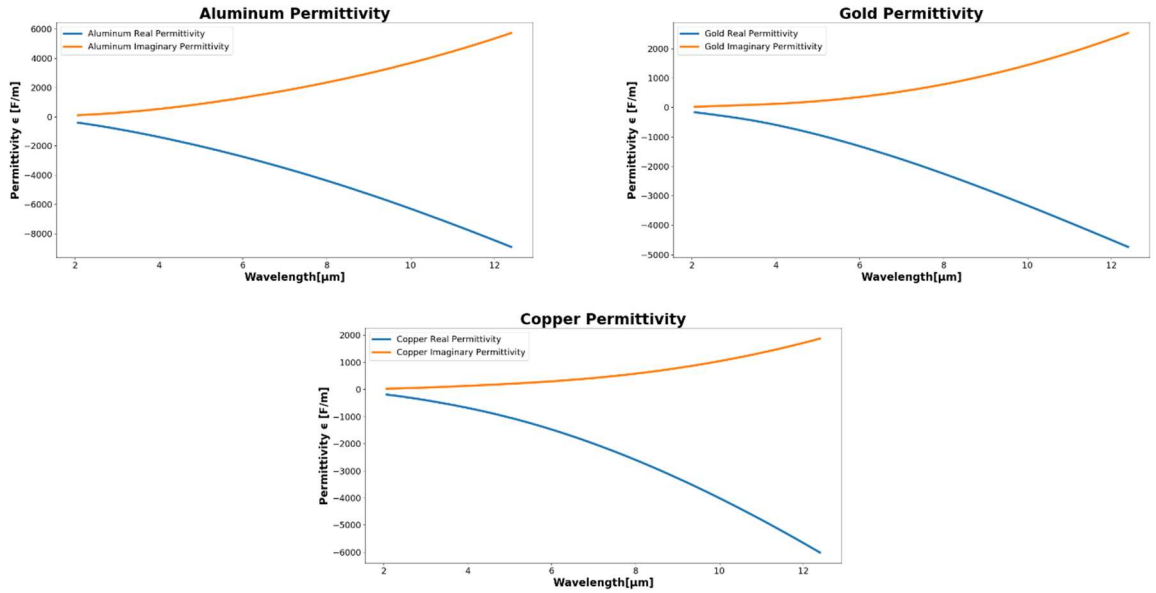

Figure 02: Permittivity for various metals being studied for use in MEMS calculated in Python using the LD model.[9]

The Brendel Oscillator (BO) model was used to calculate the permittivity of various oxide layers. The BO model also models the electron as a harmonic oscillator, but adds a Gaussian distribution to the absorption spectrum, which allows for more accurate calculation of the permittivity within various oxides, particularly in areas where the real and imaginary permittivity cross one another, such as a strong resonance that occurs within silicon dioxide around 10μm. As will be shown later, absorption resonances occur in these regions, and could be used to improve the absorption of a metasurface where at the wavelengths that these resonances are prominent. Additionally, the absorption spectra of these oxide layers must be considered for their potential interference with the desired absorption peaks the device is being designed for. The three oxide materials analyzed here are silicon dioxide, silicon nitride, and aluminum nitride. The permittivity of each oxide was calculated using Python with the BO model comprised of the following equations and the results are shown in Figure 03. [7]

$$\varepsilon(\omega) = \varepsilon_{\infty} + \sum_{j=1}^{k} X_j(\omega) \qquad (11)$$

$$X_j(\omega) = \frac{1}{\sqrt{2\pi}\sigma}\int_{-\infty}^{\infty} \exp\left(\frac{(x-\omega_{0j})^2}{2\sigma_j^2}\right) \frac{\omega_{pj}^2}{x^2-\omega^2-i\omega_{\tau j}\omega} \mathrm{dx} \quad (12)$$

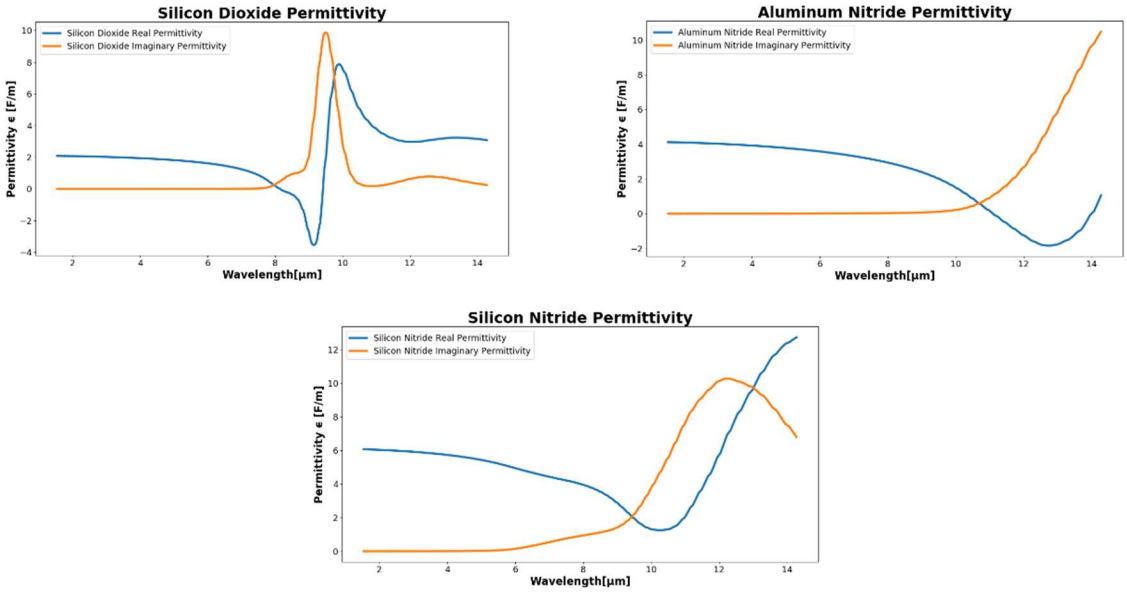

Figure 03: Permittivity for various oxides being studied for use in MEMS calculated in Python using the BO model.[7]

The properties of the metal and oxide layers calculated above were used within the circuit model approximation presented above to estimate the absorption peaks of cross shaped nano structures of varying sizes as shown in Figure 04. With the 50nm thick gold meta surface and ground plate and 200nm thick silicon dioxide spacer, the cross-length parameter 'b' is varied, and the absorption peak can be shifted significantly in its resonant wavelength. Variations in the cross-thickness parameter 'a' and unit cell size can also shift the resonant wavelength to a lesser degree, and the combination of using each of the three parameters allows the absorption peak to be tuned across a broad spectrum in the infrared range. The primary limit only being defined by the attainable feature size of the metasurface, where increasingly higher frequencies require decreasingly smaller feature sizes in order to maintain the high Q values of the subwavelength structures.

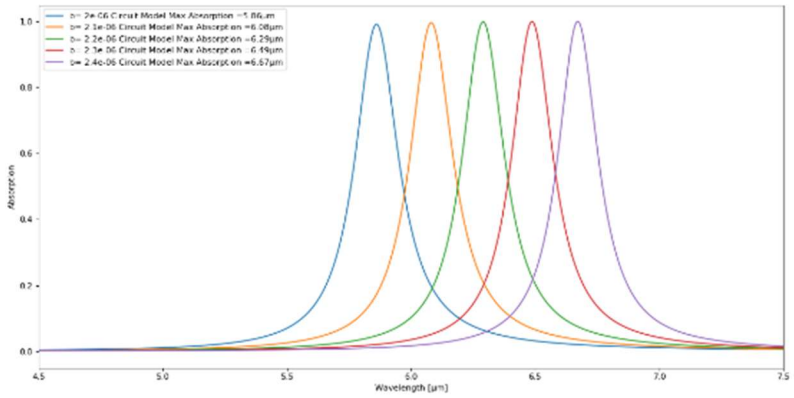

Figure 04: Absorption peaks for cross shaped nano structures using 50nm thick gold metal and 200nm thick silicon dioxide with a shifting cross length parameter 'b' calculated using Python. [5]

III. Modeling in Ansys HFSS

Periodic Floquet port simulations examine the unit cell as an infinitely periodic structure so as to ignore fringe effects, and these simulations allow us to provide an additional model to compare the results to the lumped circuit model approach presented above. The same cross shaped nano structures were simulated in Ansys HFSS with a Floquet port simulation, and the results were compared as shown in Figure 05 below. The figure shows a strong agreement with both the wavelength and intensity of the absorption peak between the Floquet port model and the circuit model using a 50nm thick gold layer, 100nm thick silicon dioxide, a cross length of 1050nm, and a cross thickness of 450nm. These values were chosen as they are the known readily achievable parameters in the currently developed lithography process to produce these devices.

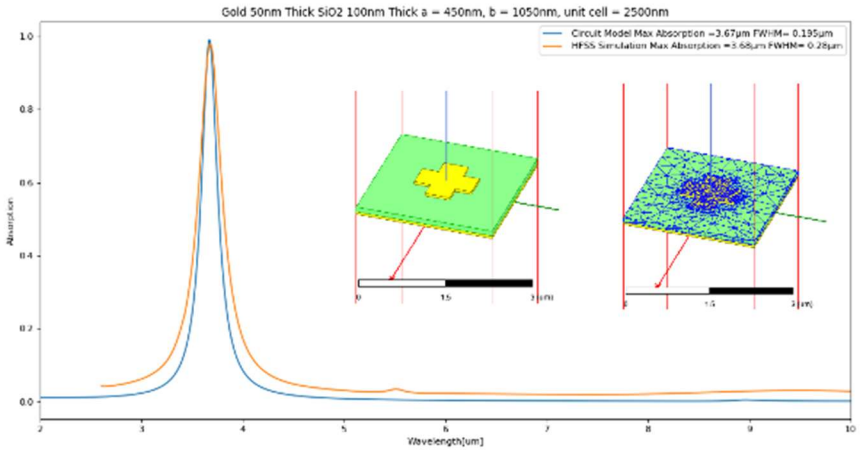

Figure 05: Metasurface Absorption with 50nm thick gold and a 200nm thick silicon dioxide dielectric spacer simulated in Ansys HFSS. [3,6]

Fully packaged devices will need passivation layers in order to protect the metal nano-surface from degradation, and the effects of these passivation layers on the absorption spectrum was explored with simulations in Ansys HFSS. Thin passivation layers of 100nm saw significant increases in the absorption of the IR spectrum near 10μm. Passivation layers typical to mass manufactured devices on the order of 1μm or larger generated significant, broad absorption peaks which cover up the absorption from the intended absorption bands. Additionally, multiple passivation layers of differing materials provided appear to further degrade device performance. Figure 06 below shows the effect of a silicon dioxide passivation layer on top of a copper metasurface. The blue curve represents the lumped circuit model approximation of the copper metasurface without a passivation layer, and the orange curve the same surface modeled in Ansys HFSS using the Floquet port model. The green curve shows the additional broadened absorption peaks around 10μm from the additional silicon dioxide passivation layer.

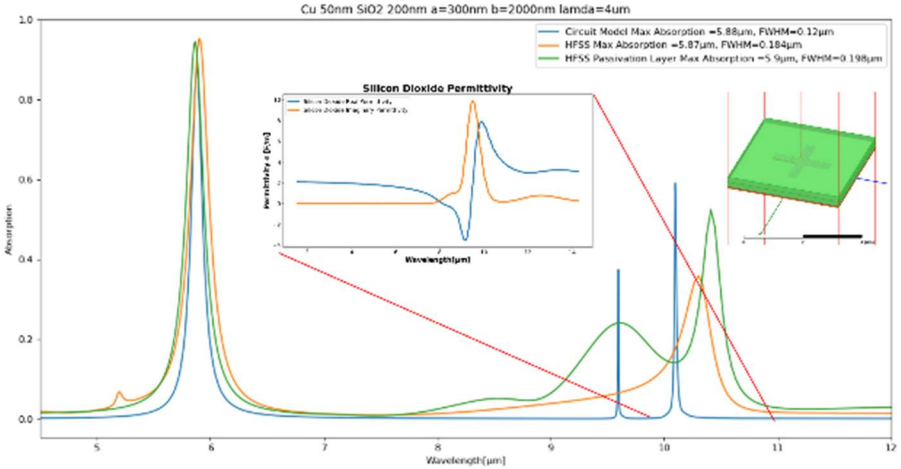

Figure 06: Metasurface absorption showing effects of a thin passivation layer of silicon nitride with a cross shaped nano surface simulated in Ansys HFSS. [3,5]

Nested ring structures were also considered in an attempt to take advantage of the formation of multiple absorption peaks. While circular rings structures would have a similar advantage of the above cross structures in being polarization independent, complicated geometries are significantly harder to manufacture. Furthermore, as the nanostructure is made smaller to achieve resonance at smaller wavelengths, the metasurface becomes crowded with metal and becomes increasingly reflective and unable to maintain sharp absorption peaks. There are also additional considerations to be made where nearby ring unit cells begin to interact with one another and create additional smaller resonances that are difficult to predict and even more complicated to correct for. Figure 07 shows the simulation of a ring structure created using Ansys HFSS with a copper ring structure nested inside of aluminum nitride. Multiple strong absorption peaks can be seen alongside additional spurious absorption peaks that were not expected and could not be easily corrected for.

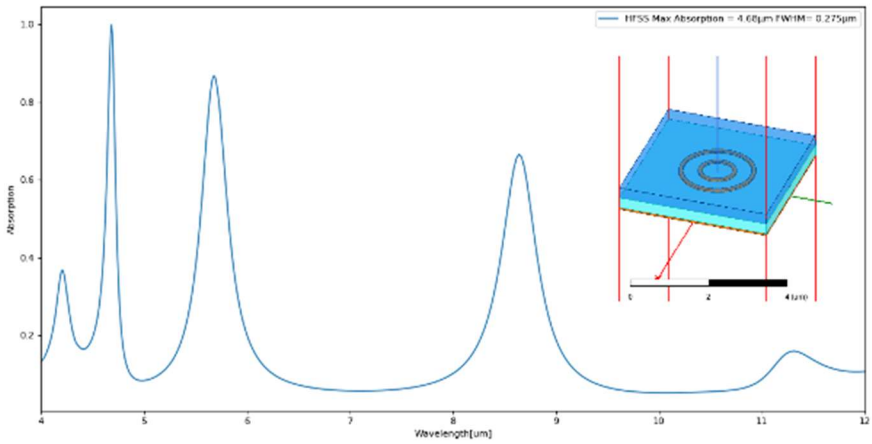

Figure 07: Metasurface absorption using a nested copper ring structure with an aluminum nitride dielectric spacer and passivation layer simulated in Ansys HFSS. [12]

Another consideration for metasurface design came in the form of Fano-resonances. Fano-resonances are structures where a plasmonic resonance in two spatial directions are made to coincide within the metasurface, creating the eponymous absorption shape described by Ugo Fano in the 1960's. Figure 08 shows a thick silicon dioxide layer with a thin gold layer on top. The plasmonic resonances in the gold will occur within the gap in the gold armature and modifying the size of the gap will allow for modification of the wavelength and strength of the peak absorption. Completing this study allowed for the determination that Fano-resonances will not be sufficient for our intended purpose, as they require lithography processes that are too small to be realized and as they rely heavily on the metasurface geometry, are not polarization independent. [9]

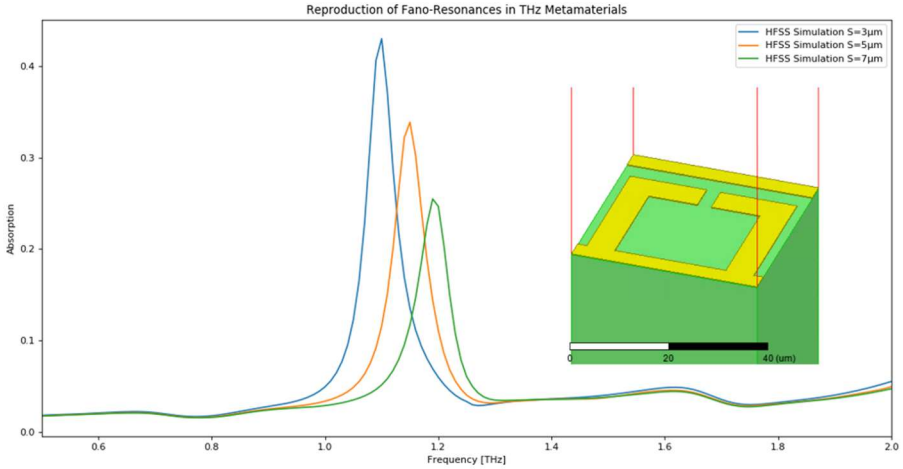

Figure 08: Metasurface absorption using Fano-resonances with a thin copper layer over silicon dioxide simulated in Ansys HFSS. [12]

IV. **Modeling in COMSOL**

Additional simulations of the metasurfaces were performed in COMSOL in order to further validate design considerations and in order to gain insight into the amount of power absorbed by the devices. The electromagnetic heating module was used to couple the losses from the incident electromagnetic radiation to the amount of power absorbed and heat generated by the metasurface. In the electromagnetic heating module, the metasurface is solved in the frequency domain, the electric fields and permittivity are updated, and then the heat transfer equation is solved in the time domain. [2]

$$\nabla \times \frac{1}{\mu}(\nabla \times E) - \varepsilon\omega^2 E = -j\omega \mathrm{J} \qquad (13)$$

$$\nabla \times \left(\frac{1}{\mu_r}\nabla \times E\right) - k_0^2\left(\varepsilon_r - \frac{j\sigma}{\omega\varepsilon_0}\right)E = 0 \qquad (14)$$

$$k_0^2(\varepsilon_r - j\sigma/\omega\varepsilon_0)E = 0 \qquad (15)$$

$$\varepsilon_r = \varepsilon_r' - j\varepsilon_r'' \qquad (16)$$

Poynting's Theorem

$$Q_{RMS} = \frac{1}{2}(\sigma \mathrm{E} \cdot E^* + \omega \varepsilon_r'' E \cdot E^* + \omega \mu_r'' B) \quad (17)$$

Heat Equation

$$\rho C_p \frac{\partial T}{\partial t} + \nabla \cdot (-k \nabla T) = Q \quad (18)$$

Figure 09 below shows the absorption of a 50nm thick gold metasurface with 200nm thick silicon dioxide spacer, with cross dimension 'a' of 650nm, and 'b' of 1900nm, with a periodicity Λ of 4µm simulated in COMSOL. This is compared to the absorption of energy from a reference plate with no metasurface on top, and the dominant electromagnetic mode can be seen underneath the metasurface, while the reference plate has only a small amount of absorption around 10µm from the silicon dioxide. Note the resonance peak at 4µm which is believed to be non-physical due to the periodicity of the simulation. The diffraction order ports are difficult to solve at wavelengths smaller than the port size and regularly generate spurious peaks that were not able to be completely eliminated within COMSOL. [2]

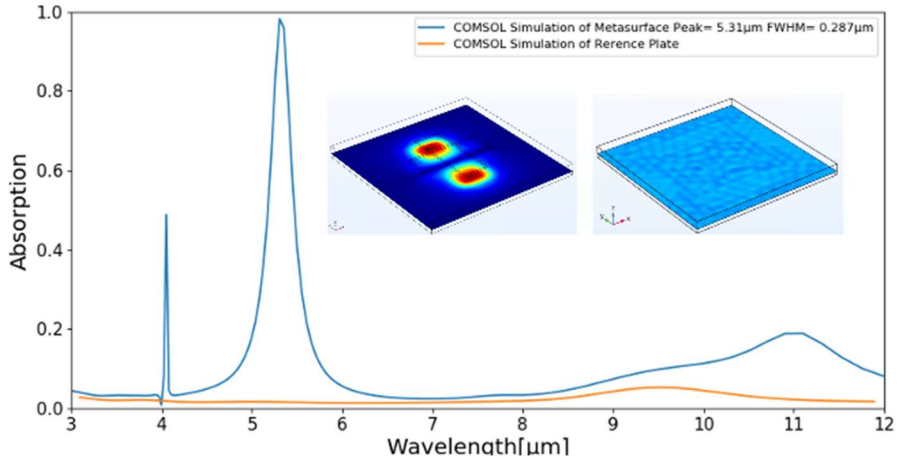

Figure 09: The blue curve represents the metasurface absorption for a 50nm gold metasurface with 200nm thick silicon dioxide, cross dimension 'a' of 650nm and 'b' of 1900nm with periodicity 4µm. The orange curve represents the absorption of a reference plate with no metasurface simulated in COMSOL.[2]

A custom 2D workspace was extruded in COMSOL based on the SEM image of the cross nanostructure in order to determine the expected effect on the absorption from the rounding of surfaces and variations that occur during lithography. The SEM image of a gold cross nanostructure with an expected cross width ‘b’ parameter of 2.6µm and a measured width of 2.504µm is shown in Figure 10.

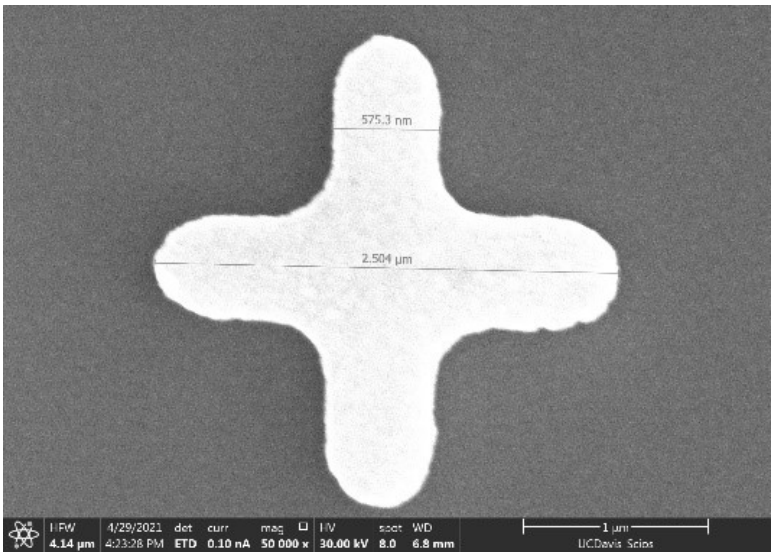

Figure 10: SEM Image of a cross nano structure with an expected ‘b’ parameter of 2.6µm and an actual measured value of 2.504µm.

After creating the workspace in COMSOL, the two absorption peaks can be compared, which shown a shift in the absorption peak caused by the variations in the cross dimensions due to the lithography of the surface. Figure 11 shows that the absorption peak shifted considerably due to the shorter and more narrow cross arms and the apparent rounding of the edges created in the lithographic process. This wavelength shift will need to be considered in the final lithographic process, and masks can be offset as necessary to tune the metasurface absorption to the necessary shift when a final, stable lithographic process is finalized.

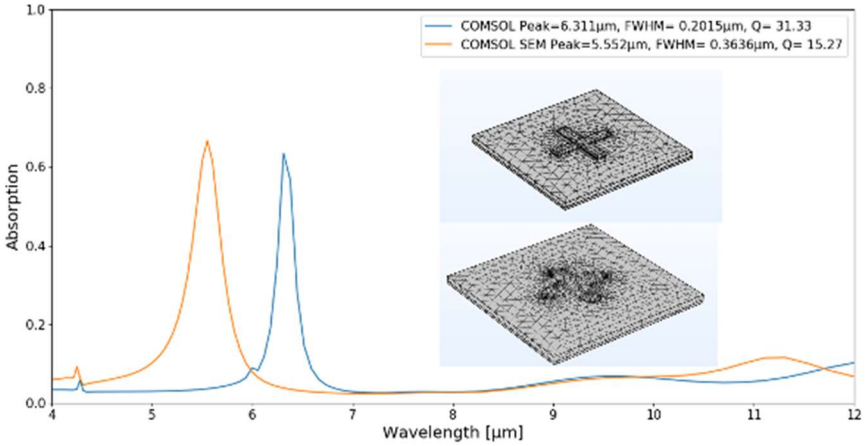

Figure 11: Metasurface absorption of two cross metasurfaces, one with ideal geometry at 2.6µm and the other at 2.504µm with rounded edges simulated in COMSOL.[2]

V. Model Comparison

The three methods of simulating the metasurfaces are compared here as shown in Figure 12 below. The three methods were each performed with a 50nm thick gold cross shaped nano structure with 100nm thick silicon dioxide, a cross width of 450nm all targeting the absorption peaks of CO2 near 4.25µm.

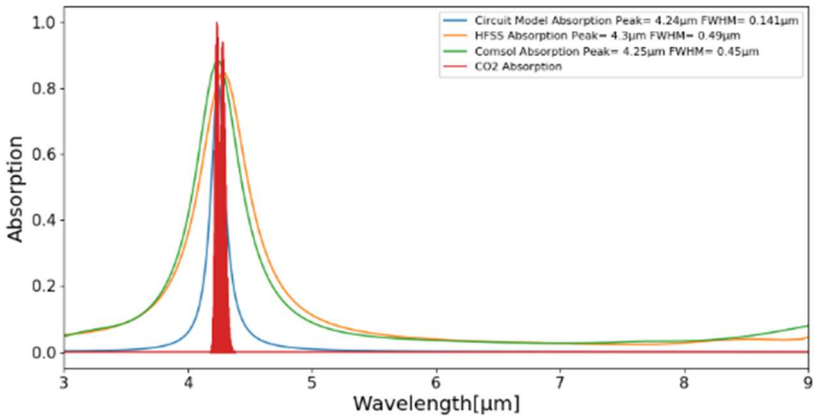

Figure 12: Metasurface absorption of a cross shaped nanostructure with 50nm thick gold and 100nm thick silicon dioxide, a=450nm, b=1450nm, and a period of 2.5µm simulated with the analytical approach described above, Ansys HFSS, and COMSOL.

VI. Experimental Measurements of Metasurfaces

a. FTIR Measurements of Metasurfaces

A repeatability assay was performed across a series of metasurfaces along a wafer to determine if there were acceptable variations across the wafer following the lithography process and to compare the physical device to the simulations. At each of the four locations along the wafer a 5x5 grid of measurements was taken with the Bruker Hyperion 2000 Fourier Transform Infrared Spectrometer. The scheme is visualized in Figure 13 below.

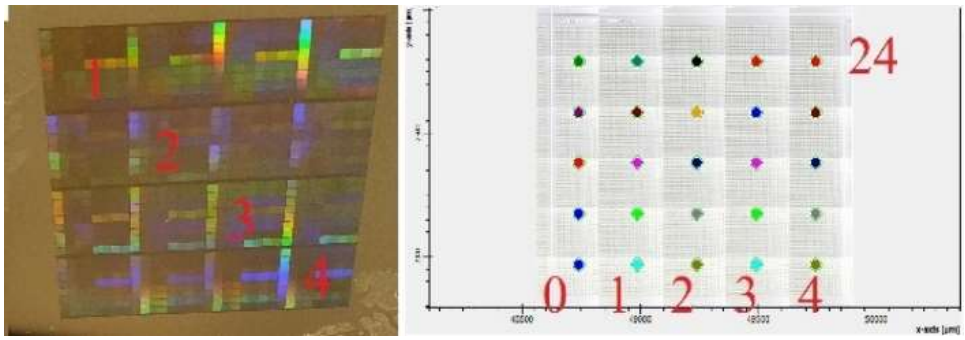

Figure 13: Images taken from the Bruker Hyperion 2000 FTIR of the four locations measured locations across the wafer (LEFT), and the 5x5 grid measured at each location (RIGHT).

The metasurfaces measured here were all 50nm thick gold cross metasurfaces with 200nm thick silicon dioxide, with varying cross thickness dimensions ‘a’, cross width dimension ‘b’ and periodicity. The assay performed for the results of one of the grid measurements is shown below in Figure 14 for a cross thickness ‘a’ of 650nm, cross width ‘b’ of 1900nm, and a periodicity of 4μm. This is presented along with an analytical circuit model simulation calculated using Python using the same cross parameters and permittivity. The measurements across each grid showed almost no variation in peak wavelength or in FWHM, with peaks varying from 5.238μm to 5.277μm where the circuit model had a peak absorption centered and 5.267μm.

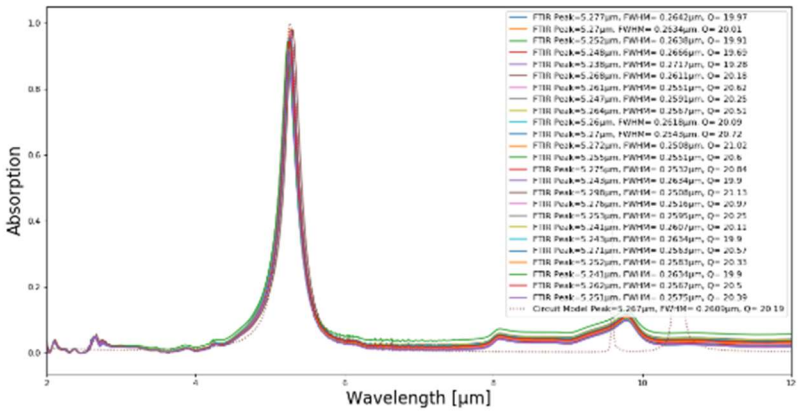

Figure 14: Metasurface absorption calculated with the analytical circuit model compared with a grid of FTIR measurements taken at various locations across a wafer.

Figure 15 shows variations across the wafer where each peak is the average of the 25-measurement grid at the four locations across the wafer labeled 1 through 4 in Figure 13, with variations in the peak of 0.2μm, while the dotted line in the figure represents the circuit model approximation predicted for the given metasurface.

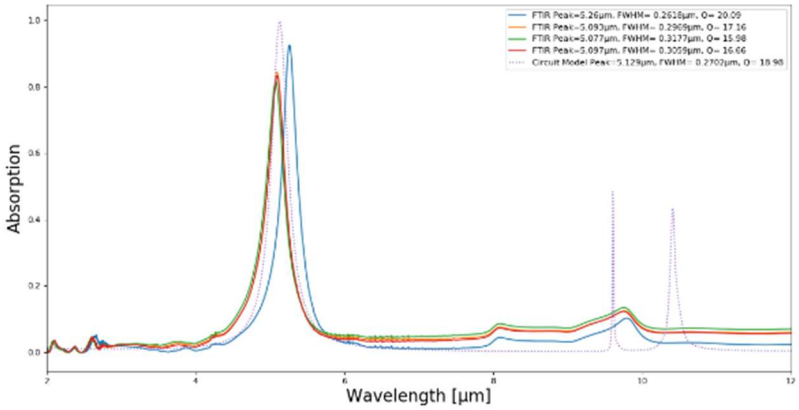

Figure 15: Dotted line represents the metasurface absorption calculated with the analytical circuit model compared with the average of the 25 FTIR measurements taken at various locations across a wafer.

The following figure shows three separate metasurfaces with 'b' cross lengths of 1600nm, 2000nm, and 2400nm alongside the absorption of each predicted by the circuit model approximation. This shows that the circuit model accurately predicts the overall shift in the peak absorption seen by increasing the cross length of the metasurface.

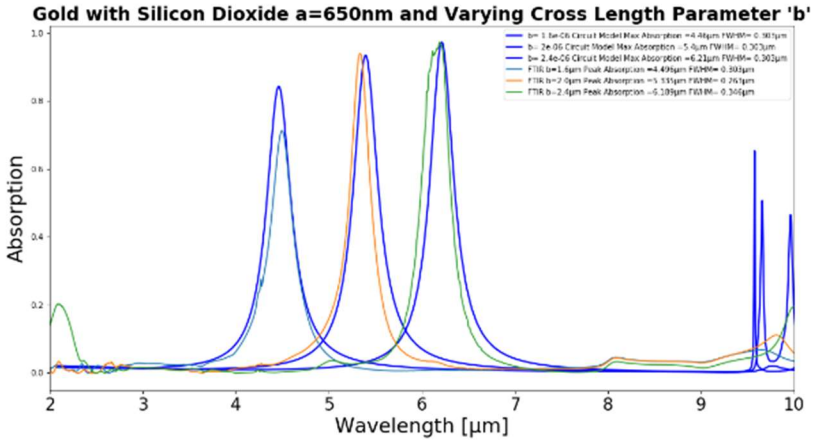

Figure 16: Metasurface absorption calculated with the analytical circuit model compared with a grid of FTIR measurements taken at various locations across a wafer.

VII. LabVIEW Experimental Setup

A LabVIEW Experiment was designed to extract the phase shift generated by a piezoelectric nanomechanical systems (NEMS) device near their resonance. The device is composed of an aluminum nitride piezoelectric baseplate 500nm thick between a 100nm platinum baseplate and a 50nm thick gold metasurface on top. The platinum baseplate is an interdigitated transducer designed to transmit energy into a higher order lateral vibrational mode, while the top gold layer is arranged into a metasurface used to absorb infrared radiation. A Bruker Hyperion Fourier transform infrared spectrometer was used to measure the absorption spectrum of the NEMS and the result is shown in Figure 17 below. [5]

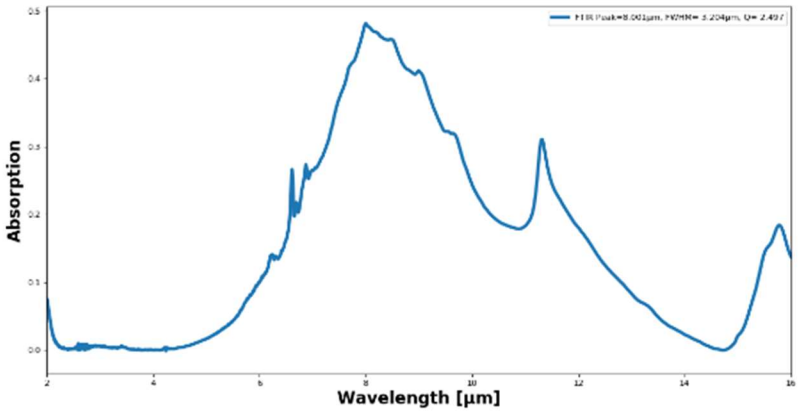

Figure 17: FTIR Measurement of NEMS device measured with the Bruker Hyperion 2000.

The device was placed into an optical setup as shown in Figure 18. A 780nm laser is reflected off of gold sample plate, rotated though a polarizing crystal, and then sent to a focusing lens. A beam splitter is also present before the focusing lens to direct the power onto an infrared power meter to determine the amount of power incident on the device. While the infrared radiation is incident on the NEMS device, a function generator is sending a microwave pulse which is reflected from that port back to a directional coupler to measure the phase shift generated by the piezoelectric response.

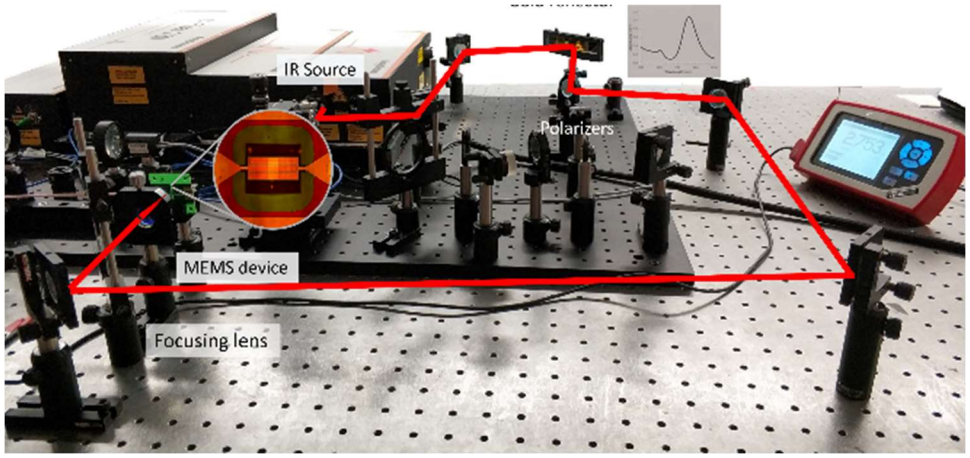

Figure 18: Beam path of the IR laser with reflection from the sample on a gold reflector, through a polarizing crystal, and onto the MEMS device.

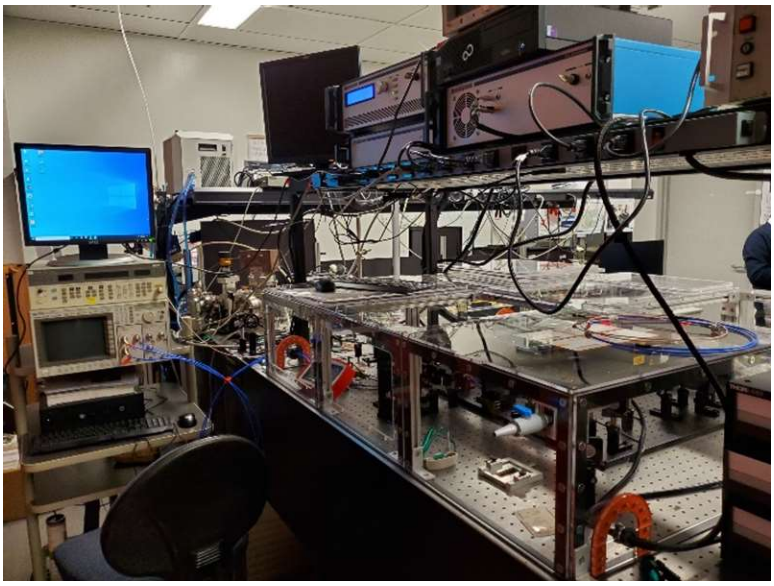

Figure 19: Full experiment showing the LabVIEW control computer on the left, and the experiment enclosure on the right.

Figure 19 above shows the optical bench with the laser in the laboratory, and Figure 20 describes the LabVIEW control of the various pieces of equipment. The Menlo Systems TeraK15 780nm laser excites the samples and the NEMS device. Data analysis can be performed while collection continues within LabVIEW or exported as data files. The HP Agilent 8657B function generator allows signals up to 1.03 GHz at +13dBm (~1.5Vpeak). An HP Agilent 54750A oscilloscope reads DC to 2.5 GHz with 40mV sensitivity at 150MHz. A Thorlabs PM100D power meter measures the power of incident infrared radiation from 700-1600nm with μW sensitivity. The LabJack T4 analog to digital converter has a 12-bit resolution and 4 input pins ranging from 0-2.5V (ideal 0.6mV) and 4 input pins 0-10.0V (ideal 2.4mV). In conjunction with a low pass filter and a phase detection circuit, the phase difference can be measured both from the oscilloscope data taken at each measurement and confirmed with the DC voltage output from the phase detector. Last, a rotational motor for mounted polarizers have a minimum 0.05-degree rotational motion allowing for a resolution of incident power of 0.1μW. Previously, a lab technician would need to be present for each frequency data point that needs to

be taken, but with the setup described here, hours of data capture is possible with minimal user input necessary.

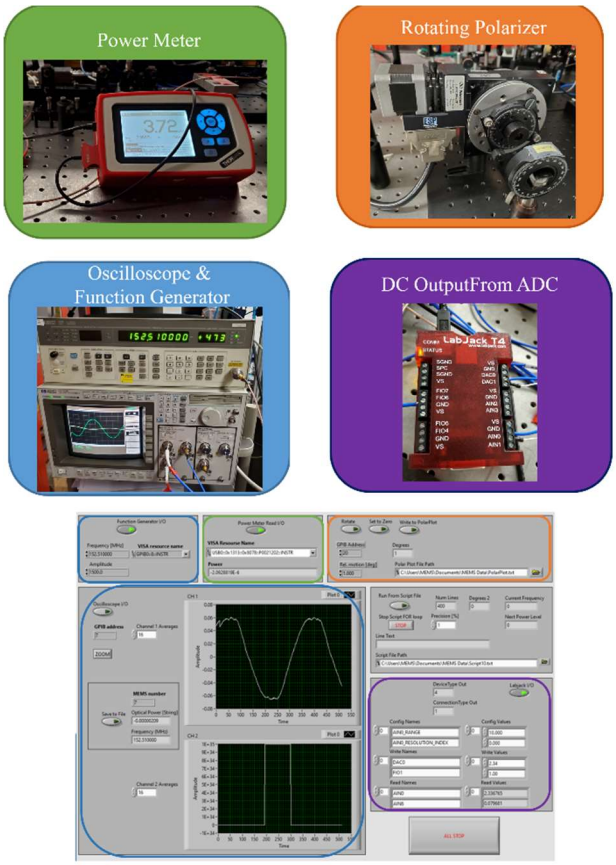

Figure 20: LabVIEW control panel showing controls for the function generator an oscilloscope (BLUE, BOTTOM LEFT), power meter (GREEN, TOP LEFT), rotating polarizer (ORANGE, TOP RIGHT), and analog to digital converter (PURPLE, BOTTOM LEFT).[8]

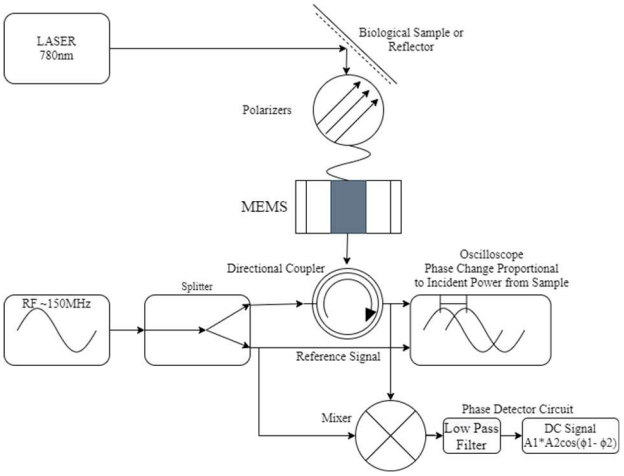

Figure 21: LabVIEW experiment diagram.

Figure 22 describes a control loop implemented within LabVIEW which sends a frequency to the piezoelectric NEMS, and then determines the amount of power incident on the device from the infrared power meter. The control loop then rotates the polarizing mount until the power incident is within the desired accuracy set by the user and continues the loop until all of the frequency point have been measured, saving the data from the oscilloscope, power meter, and DC input for each iteration of the loop.

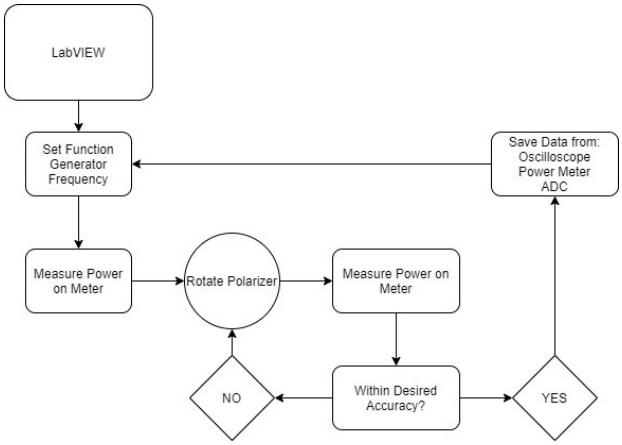

Figure 22: LabVIEW control loop for automating data collection.

Figure 23 verifies the functionality of the LabVIEW systems ability to collect the necessary data using the function generator and oscilloscope, and to focus the necessary power onto the MEMS device. The current system can take in a script file using an arbitrary number of frequencies and desired power levels ranging from 10μW to 10mW, and then collect the output waveform every 20 to 30 seconds without user input. The system was capable of functioning for several hours, taking thousands of data points without any user input.

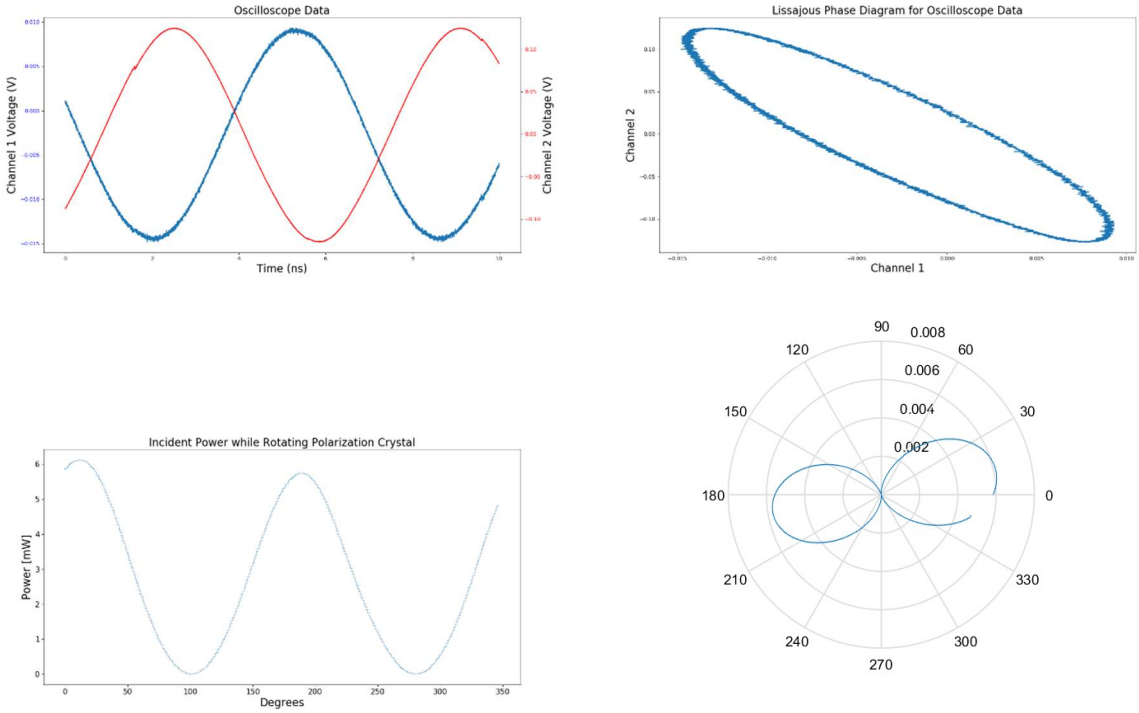

Figure 23: Oscilloscope data (TOP LEFT) and Lissajous diagram (TOP RIGHT) collected from the oscilloscope in LabVIEW. Incident power while rotating the polarization crystal (BOTTOM LEFT), and a polar plot of the data (BOTTOM RIGHT).

A python script is used to extract the waveforms at each frequency, curve fit to a sinusoidal curve, and output the phase of both waveforms at each frequency. At this time the expected phase shift from the nanomechanical resonator is not being seen in the data, and it's unclear if a strong enough signal is being received or if there are issues with the devices that are currently available. New, functional devices were not available at the time of this research to confirm this.

VIII. Gas Sensing

The high-resolution transmission molecular absorption database HITRAN was used to analyze the absorption peaks for various gases that may be of interest for detection using this technology, and also to determine the amount of power absorbed by a column of gas. Beer

Lambert's Law is used in conjunction with the database to determine the exponential decay of the transmittance through a column of gas of length x.

$$T = e^{-k_\nu x} \qquad (19)$$

Where the extinction coefficient is defined as:

$$k_{ij}(\nu,T,p) = S_{ij}(T)\, f(\nu;\nu_{ij},T,p) \qquad (20)$$

S_{ij} is the spectral line intensity in wavenumber per column density from HITRAN – with a temperature dependence determined by:

$$S_{ij}(T)=S_{ij}(T_{ref})\frac{Q(Tref)}{Q(T)}\frac{\exp(-c_2E''/T)}{\exp(-c_2E''/Tref)}\frac{[1-\exp(-c_2\nu_{ij}/T)]}{[1-\exp(-c_2\nu_{ij}/Tref)]} \qquad (21)$$

A normalized line shape function is given by $f(\nu;\nu_{ij},T,p)$ with a Lorentzian profile in the lower atmosphere near room pressure, and a Gaussian profile at low pressure in the upper atmosphere.

$$\gamma(p,T)=(Tref/T)^n(\gamma_{air}(p_{ref},T_{ref})(p-p_{self})+\gamma_{self}(p_{ref},T_{ref})p_{self}) \qquad (22)$$

Where Q, c_2, γ_{air}, $\delta(p_{ref})$, γ_{self} , E" are available for download from the HITRAN database.[11]

Python was used to analyze information from the HITRAN database to determine the most common gases prevalent in the atmosphere for which peaks might be capable of being targeted by the MEMS devices presented here. The absorption spectra for various molecules of interest in shown below in Figure 24.

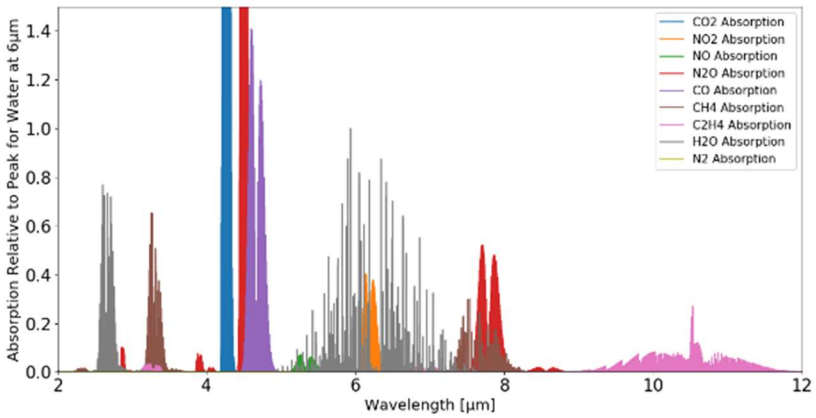

Figure 24: Absorption peaks of various gases relative to the peak absorption of water at µm.

The spectral absorption peaks for CO_2 are shown in Figure 25 below along with circuit model approximation metasurfaces used to target absorption at the same wavelengths.

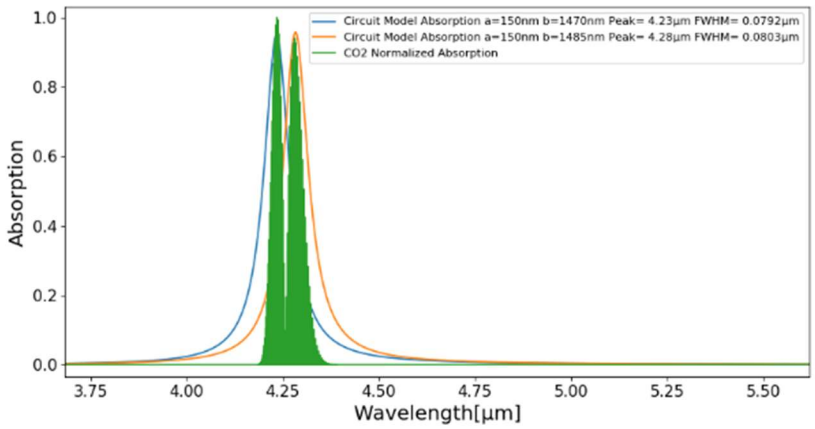

Figure 25: Spectral absorption of CO_2 near 4.25µm in green, with two metasurfaces designed with the circuit model approximation targeting those bands.

Future work on this project will switch from a fixed 780nm laser source to using blackbody radiators to more realistically simulate the heat generated by objects to compare against. Figure 26 presents a blackbody radiator at 1200 degrees Celsius, and the energy absorbed by a metasurface targeting the 4.25µm peak of CO_2, as well as the energy absorbed by a column density of CO_2 across all of its spectral lines.

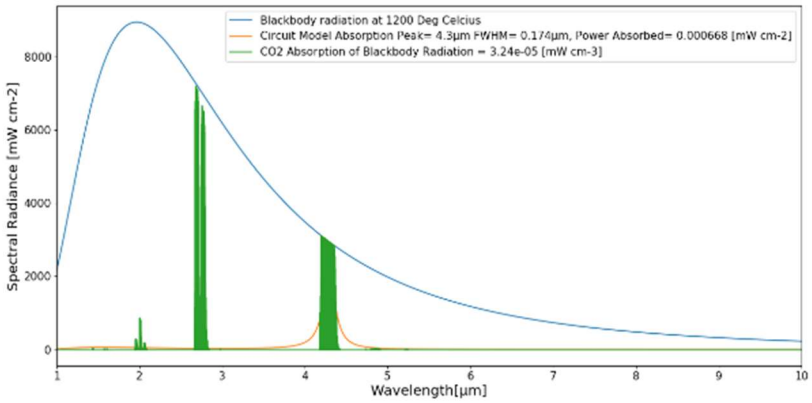

Figure 26: Emission from a blackbody radiation (blue) being absorbed by a metasurface (orange) and a column density of carbon dioxide (green).

IX. Biological Sensing

There are also very promising prospects for the technology presented here to be applied to infrared sensing on biological subjects. With assistance from the Carney labs at UC Davis a number of biological samples were collected, some of which exhibit signs of squamous cell carcinoma, skin cancer. An example of one of these samples as viewed with the Bruker Hyperion microscope is shown in Figure 27.

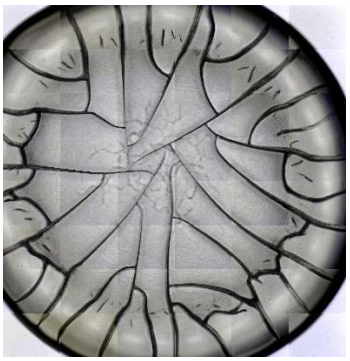

Figure 27: Oscilloscope data and Lissajous diagram collected from the oscilloscope in LabVIEW.

A collection of 19 cancer samples with 9 control samples were initially measured, and the results of the FTIR measurements are shown in Figure 28 below as prepared by another student in the research group, Antonio Guillén Pérez. This research intends to apply machine learning

algorithms to identify the number and FWHM of metasurfaces needed to positively identify a positive or negative sample after training.

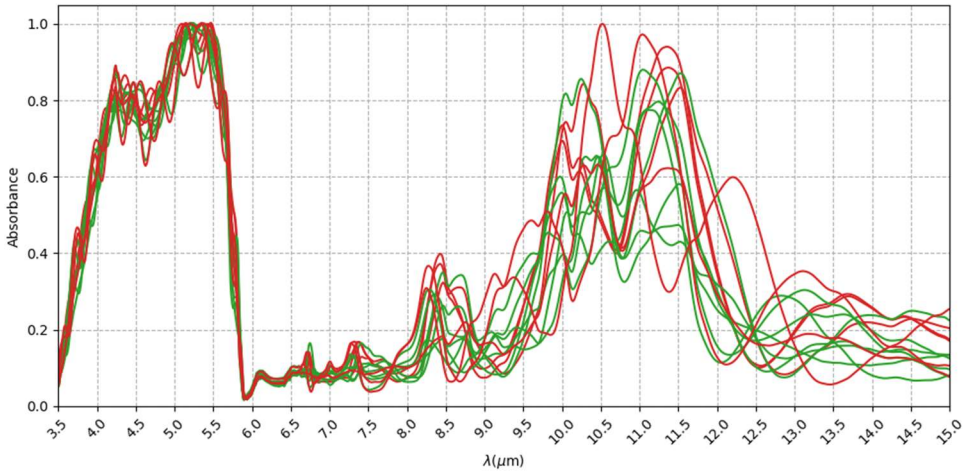

Figure 28: Cancer positive samples (red) and cancer negative samples (green) for various FTIR measurements of biological samples prepared by Antonio Guillén Pérez.

X. Future Work and Next Steps

Future work in this research will require finishing the measurement of newly produced NEMS devices to determine if the LabVIEW experimental setup is sensitive enough to measure the phase shift generated by the devices. Setup of the blackbody radiator will also provide further insight to how the devices function with a standard infrared radiation source rather than a monochrome laser, which will be a very useful piece of information to bring the devices closer to their real-world applications. Additionally, the COMSOL and HFSS simulations must be modified in order to eliminate spurious modes that occur at wavelengths shorter than the port size so that higher frequency simulations can be performed. Lithographic processes used to produce these MEMS can be modified to consider the shift in peak absorption due to variances in material deposition. Further research into machine learning will provide our research group with

the number of metasurfaces that are necessary to adequately identify a given gaseous or biological sample.

XI. CONCLUSIONS

Experimental measurements and various simulations all confirm that the MEMS and NEMS systems presented above have successfully met to criteria to act as low cost, uncooled, fast, high resolution infrared detectors for the sensing of biological and gaseous samples. The circuit model approximation is an easy and powerful tool to determine the initial feature sizes of metasurfaces, and the COMSOL and HFSS simulations can be quickly run to confirm these values. Each of these simulations have strong agreement with the final absorption peaks of the metasurfaces produced by the current lithographic process used to make these devices. Gold and silicon dioxide offer the best performance, while aluminum and aluminum nitride are offering a much cheaper alternative that may be able to meet the necessary criteria as well. Additional refinement is needed to reach higher frequencies and sharper absorption peaks and the experimental setup developed here will be able to assist in that process.

ACKNOWLEDGEMENTS

Thank you to the other members of the research team in the Applied Micro/Nano-Electromagnetics Research Laboratory Melissa Gulseren, Trevor Pollack, and Matthew Benson for their assistance on the project. Many thanks for the assistance from Victor Chiu of the Carney Lab here at UC Davis. Also, thank you to Sebastián Cánovas Carrasco from the Universidad Politécnica de Cartagena for his help in introducing me to the project.

Thank you to the team at Texas Instruments, especially Jeronimo Segovia-Fernandez, for their providing me the opportunity to contribute to their project and for their assistance and feedback on my work.

A very special thanks to Professor Juan Sebastian Gomez-Diaz, Professor at UC Davis, for his support and guidance throughout my graduate studies.

REFERENCES

[1] J. Brückner, J. Rouzo, L. Escoubas, G. Bergine, O. Calvo-Perez, N. Vukadinovic, F. Flory, "Metamaterial filters at optical-infrared frequencies," Optics Express, 2013.

[2] COMSOL Multiphysics 5.5 (2020). COMSOL.

[3] Electronics Desktop – HFSS. (2020). Ansys.

[4] Y. Hui, J. S. Gomez-Diaz, Z. Qian, A. Alu, M. Rinaldi, "Plasmonic piezoelectric nanomechanical resonator for spectrally selective infrared sensing," Nature Communications. 7:11249, 2016.

[5] Y. Hui, S. Kang, Z. Qian, M. Renaldi, "Uncooled infrared detector based on an aluminum nitride piezoelectric fishnet metasurface," Journal of Microelectronic Systems, IEEE, 2021.

[6] S. Kang, Z. Qian, V. Rajaram, S.D. Calisgan, A. Alu, M. Rinaldi, "Ultra-Narrowband Metamaterial Absorbers for High Spectral Resolution Infrared Spectroscopy," Advanced Optical Materials. 7, 1801236, 2019.

[7] J. Kischkat, S. Peters, B. Gruska, M. Semstiv, M. Chashnikova, M. Klinkmüller, O. Fedosenko, S. Machulik, A. Aleksandrova, G. Monastyrskyi, Y. Flores, W. T. Masselink, "Mid-infrared optical properties of thin films of aluminum oxide, titanium oxide, silicon dioxide, aluminum nitride, and silicon nitride," Applied Optics, 2012.

[8] LabVIEW (2020). National Instruments.

[9] Z. Li, S. Cakmakyapan, B. Butun, C. Daskalaki, S. Tzortzakis, X. Yang, E. Ozbay. "Fano resonances in THz metamaterials composed of continuous metallic wires and split ring resonators," Optics Express, 2014.

[10] A. Rakic, A. Djurisic, J. Elazar, M. Majewski, "Optical properties of metallic films for vertical-cavity optoelectronic devices," Applied Optics, 1998.

[11] L. S. Rothman, *et al.*, "The HITRAN 2012 Molecular Spectroscopic Database", *J. Quant. Spectrosc. Radiat. Transfer* 130, 4-50 (2013).

[12] X. Shen, T.J. Cui, J. Zhao, H.F. Ma, W.X. Jiang, H. Li, “Polarization-independent wide-angle triple-band metamaterial absorber,” Optics Express, 2011.